Applied Catalysis B: Environmental 148–149 (2014) 91–105

Contents lists available at ScienceDirect

Applied Catalysis B: Environmental

journal homepage: www.elsevier.com/locate/apcatb

Hydrogen from biogas: Catalytic tri-reforming process with Ni/La—Ce—O mixed oxides

Lidia Pino*, Antonio Vita, Massimo Laganà, Vincenzo Recupero

CNR Institute of Advanced Technology for Energy "Nicola Giordano", Via S. Lucia 5, 98126 Messina, Italy

ARTICLE INFO

Article history:
Received 15 July 2013
Received in revised form 7 October 2013
Accepted 21 October 2013
Available online 28 October 2013

Keywords:
Biogas
Tri-reforming
Hydrogen production
Syngas
$Ni/La_2O_3–CeO_2$ catalysts

ABSTRACT

A series of Ni catalysts supported on La—Ce—O mixed oxides with different Ni content ($Ce_{1-3x}La_{2x}Ni_xO_{2-\delta}$, $x = 0.10$; 0.20 and 0.25) prepared by combustion synthesis, was tested in tri-reforming reaction of simulated biogas. The influence of O_2/CH_4, CH_4/CO_2 molar ratios in the reaction stream has been evaluated caring out the reaction at 800 °C, under a fixed gas hourly space velocity (GHSV = 31,000 h^{-1}). The highest catalytic activity was obtained with the $Ce_{0.70}La_{0.20}Ni_{0.10}O_{2-\delta}$ sample that showed high stability (CH_4, CO_2 conversion rates and the H_2/CO molar ratio in the reformed gas were 1.56 mmol/s g_{Ni}, 0.56 mmol/s g_{Ni} and 1.57, respectively) under an average biogas composition ($CH_4/CO_2 = 1.5$). No carbon deposition was detected after 150 h of reaction.

The characterizations of the samples have highlighted that Ni and La ions were partially incorporated into CeO_2 framework, cubic fluorite structure of CeO_2 support was retained also at high level of doping. Ni metal phase in close contact with $La_2O_3–CeO_2$ matrix coupled with Ni^{2+} with high cationic character appeared to be responsible of the catalytic activity and stability of the catalysts.

1. Introduction

Hydrogen is considered a clean carrier for sustainable energy production [1,2]. It can be widely used in the power and chemical industries; besides, can be efficiently converted to electricity via the appropriate fuel cells systems with zero emissions of greenhouse gases or hazardous species [3,4]. Currently hydrogen production process includes steam reforming (SR), partial oxidation (POX) and autothermal reforming (ATR) of hydrocarbons. Recently "tri-reforming process" is receiving growing attention [5–8], it was proposed initially for the utilization of power plant flue gas producing synthesis gas without the need of CO_2 pre-separation step [9,10]. Typical flue gas contains CO_2, H_2O, O_2 and N_2 mixture, adding to these effluents CH_4 and eventually H_2O and air a reaction mixture results that proceeds with adequate rate in a temperature range of 700–900 °C in presence of a proper catalyst [11,4]. The process involves a combination of dry reforming (Eq. (1)), steam reforming (Eq. (2)) and partial oxidation of methane (Eq. (3)) in a single step, producing syngas with the desiderate H_2/CO ratio by altering the relative amounts of the reagents:

$$CO_2 + CH_4 \rightarrow 2CO + 2H_2 \qquad \Delta H^\circ_{289} = 247.3\ \text{kJ/mol} \tag{1}$$

$$H_2O + CH_4 \rightarrow CO + 3H_2 \qquad \Delta H^\circ_{298} = 206.3\ \text{kJ/mol} \tag{2}$$

$$CH_4 + 0.5O_2 \rightarrow CO + 2H_2 \qquad \Delta H^\circ_{298} = -36.6\ \text{kJ/mol} \tag{3}$$

The uniqueness of the tri-reforming process is that waste harmful gases (i.e. flue gas from fossil fuel fired power plants, biogas from anaerobic digestion of biomass, landfill gas etc.) can be utilized as raw material [12]; the addition of appropriate amount of methane (or natural gas), oxygen and steam, on the basis of the gas composition and in order to rule the H_2/CO ratio in the reformed gas, allows to obtain synthesis gas for fuel cells and/or for all those process requiring syngas (ammonia, methanol, dimethyl ether, Fischer–Tropsch synthesis process) [13,14].

The absence of CO_2 separation step makes the process an interesting application to mitigate (in term of $gCO_2/kW_{produced}$) the CO_2 emissions; the presence of H_2O and O_2 in the reaction's stream help to mitigate the carbon deposition phenomena (Eqs. (4)–(8)), major drawback of dry reforming reaction

$$CH_4 \rightarrow C + 2H_2 \qquad \Delta H^\circ = 74.9\ \text{kJ/mol} \tag{4}$$

$$2CO \rightarrow C + CO \qquad \Delta H^\circ = -172.2\ \text{kJ/mol} \tag{5}$$

$$C_{ads} + CO_2 \rightarrow 2CO \qquad \Delta H^\circ = 172.2\ \text{kJ/mol} \tag{6}$$

$$C_{ads} + H_2O \rightarrow CO + H_2 \qquad \Delta H^\circ = 131.4\ \text{kJ/mol} \tag{7}$$

* Corresponding author. Tel.: +39 90624232; fax: +39 90624247.
E-mail address: lidia.pino@itae.cnr.it (L. Pino).

0926-3373/$ – see front matter © 2013 Elsevier B.V. All rights reserved.
http://dx.doi.org/10.1016/j.apcatb.2013.10.043

$$C_{ads} + O_2 \rightarrow CO_2 \qquad \Delta H^\circ = -393.7\,kJ/mol \tag{8}$$

and, at the same time, the added O_2 makes less endothermic the total process.

In this context, the application of tri-reforming reaction to biogas, renewable source of CH_4 and CO_2, for the hydrogen production can promote the recycling concept in the society, increasing the use of this greenhouse gases. The term biogas generally includes the gas produced by the anaerobic digestion or fermentation of any biodegradable organic matter including manure, sewage, sludge etc. It has a typical composition of 50–70 vol% CH_4, 25–45 vol% CO_2 along with small amounts of N_2, O_2, H_2S, as well as traces of NH_3 with organic and element-organic compounds [15,16].

The direct biogas conversion to synthesis gas by tri-reforming process emerges as a technically simple and flexible option; the harmful contaminants must be removed from biogas before the reforming step, to prevent the poisoning of the reforming catalysts [17,18]. Moreover, since the biogas composition can fluctuate according to factors such as the properties or amount of wastes, whereby it is important that the reforming catalyst can operate at different CH_4/CO_2 ratios with stable performance. As widely reported in literature, the catalysts that are employed in the reforming process range from noble metal (Rh, Ru, Pt, Pd, Ir) [19–24] to base metal (Ni, Co) supported over metal oxides, mixed oxides and perovskites [25–27]. Particular attention is devoted to the development of non-noble metal catalysts, due to high cost and limited availability of noble metals. Nickel-based catalysts are the most investigated catalytic systems, despite they may be quickly deactivated by coking. Redox support materials, such as ceria-based solid solutions, or mixed oxides to disperse the active Ni content are generally employed to mitigate the catalyst deactivation by carbon deposition. Ni-based catalysts have been applied, in the recent literature, to tri-reforming reaction. The effect of different supports (MgO, CeZrO, CeO_2, ZrO_2 and La_2O_3) on the Ni activity has been evaluated by Song and Pan [8]. From the reported study emerges that the higher interface between Ni, MgO and ZrO_2, resulting from $NiO/ZrO_2/MgO$ solid solution, promotes CO_2 and H_2O adsorption, leading to an increase of CO_2 converted with stable performance of the catalyst during 5 h of reaction. Analogous catalytic system has been applied by Walker et al. [6]; the catalyst containing 8% of Ni and Mg impregnated on $Ce_{0.6}Zr_{0.4}O_2$ shows a minimal deactivation under different reagents composition. Jiang et al. [28] have highlighted as the moderate metal–support interactions and the ability to be reduced can contribute to the high stability of $Ni/Mg_{0.75}Ti_{0.25}O$ and $Ni/Mg_{0.50}Ti_{0.50}O$ catalysts. García-Vargas et al. [8] have shown that the strong metal–support interactions between Ni and support (β-SiC) can inhibit the deactivation process; good catalyst stability has been obtained along 250 min of test.

In our previous study we have observed that the addition of appropriate amount of La (La/Ni = 2, atomic ratio) to the catalytic Ni/CeO_2 system (1.76 wt%) can improve the catalytic activity for methane tri-reforming reaction [29]. In the present note Ni/Ce—La—O mixed oxides with a La/Ni molar ratio of 2 are used as model catalysts; the effect of Ni load, molar ratios O_2/CH_4 and CH_4/CO_2 in the feed, on their catalytic performance and stability in tri-reforming reaction of simulated biogas is evaluated. X-ray diffraction (XRD), H_2-temperature programmed reduction (TPR), BET surface area, transmission electron microscopy (TEM), scanning electron microscopy coupled with energy dispersive X-ray diffraction (SEM–EDX) and X-ray photoelectron spectroscopy (XPS) were used to observe the characteristics of the prepared catalysts. The carbon formation and amount in the used catalysts were examined by SEM, temperature programmed hydrogenation (TPH) and CHNS elemental analysis, respectively.

2. Experimental

2.1. Catalyst preparation

Ni-based catalysts supported on Ce—La—O mixed oxides were prepared by combustion synthesis, details of the preparation procedure have been previously reported [29]; the related Ni content ranges between 3.66 and 10.25 wt%, while the La/Ni mole ratio was maintained constant (La/Ni = 2). For simplicity, a general formula of $Ce_{1-3x}La_{2x}Ni_xO_{2-\delta}$ (x = 0.10; 0.20 and 0.25) with x that denotes the molar fraction of Ni, is used throughout the present study. Generally the stable Ce ↔ Ni exchange within the fluorite lattice shows a limit of 10–20%, for higher Ni concentrations the formation of $NiO/Ce_{1-x}Ni_xO_{2-\delta}$ mixtures can be observed [30]. As in the current catalysts the Ni content exceeds this limit, the double notation as supported (wt%) and as solid solution is reported. The "as prepared" catalysts were treated in O_2 at 400 °C for 1 h in order to remove the carbon residue from combustion synthesis; then pelletized, crushed and sieved (200–600 μm) have been tested after a pre-reduction step carried out at 450 °C in a flow of 50% H_2/N_2 mixture.

2.2. Catalysts testing

The tri-reforming reaction (TRF) of simulated biogas was evaluated using 500 mg of catalyst packed in a tubular fixed bed quartz reactor (i.d. = 0.6 cm) at 800 °C with a gas hourly space velocity (GHSV) of 31,000 h^{-1} under atmospheric pressure. Heating of the reactor was provided by an oven, in which is inserted the reactor, controlled by a programmable temperature controller. The temperature of the catalytic bed was measured by a K-type thermocouple placed within a quartz capillary well in the middle part of the bed. The gaseous feeds (CH_4, CO_2, O_2 and N_2 as internal standard) were controlled by mass flow controllers; steam was added to the feed by using an isocratic pump (Agilent 1100 Series) and a properly designed evaporator. The reactor effluents were analyzed by a gas-chromatograph (Agilent 6890 Plus) equipped with a FID and TCD. The activity tests were performed at constant H_2O/CO_2 molar ratio (H_2O/CO_2 = 1) by changing the O_2/CH_4 molar ratio (from 0.05 to 0.10) or the CH_4/CO_2 ratio (from 1.04 to 2.47), respectively.

On-line chromatographic analysis of the reaction products, stabilized for 0.5 h, was carried out every 20 min during each test; typical duration of each catalytic test was 6 h. Stability test was also carried out at 800 °C for 150 h. The reactants conversion, reaction rate (r_{react}, mmol/s g_{Ni}) and the catalysts deactivation where calculated according to the following equations:

$$\text{Reactant}_{conv} = \frac{F_{react,in} - F_{react,out}}{F_{react,in}} \times 100$$

$$r_{react} = \text{Reactant}_{conv} \times \frac{F_{react,in}}{W_{Ni}}$$

$$\text{Deact.} = \frac{X_{CH_4}^{0.5h} - X_{CH_4}^{6h}}{X_{CH_4}^{0.5h}} \times 100$$

where F is the molar flow rate of reagents species measured at inlet or at outlet of the reactor, W_{Ni} is the weight (g) of the nickel in the catalysts, X_{CH_4} represents the CH_4 conversion after 0.5 and 6 h of reaction, respectively. The pressure drop across the catalysts bed, indicator of the carbon deposition, was measured as function of the time-on-stream.

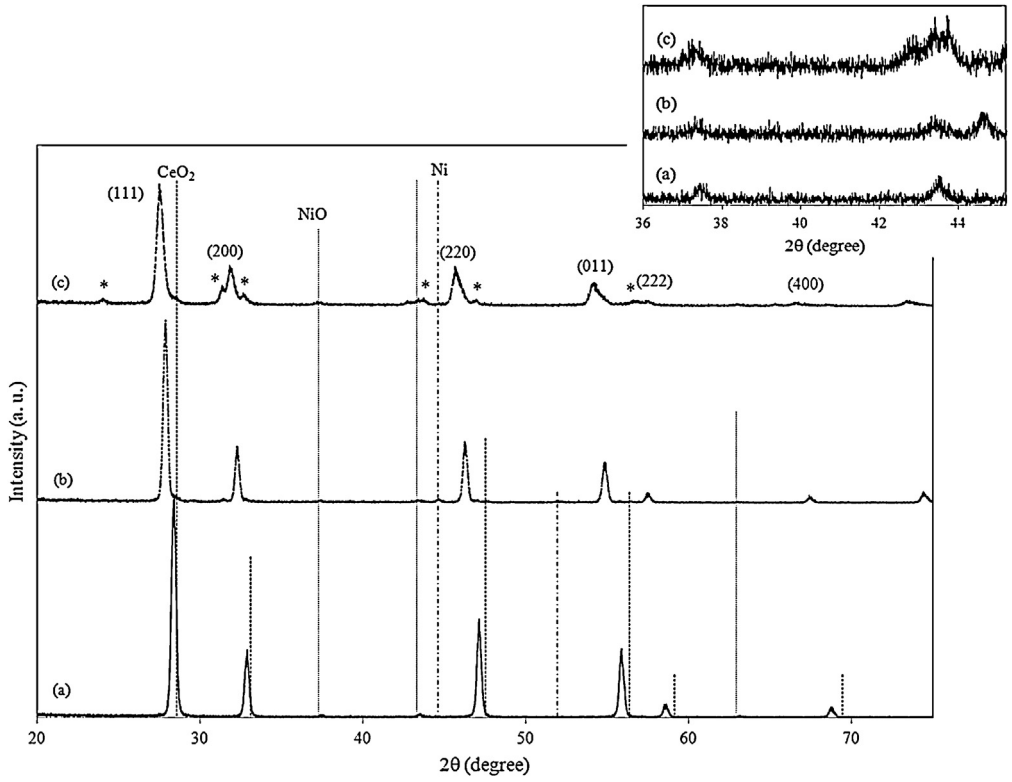

Fig. 1. XRD patterns of the different catalysts: (a) $Ce_{0.70}La_{0.20}Ni_{0.10}O_{2-\delta}$; (b) $Ce_{0.40}La_{0.40}Ni_{0.20}O_{2-\delta}$; (c) $Ce_{0.25}La_{0.50}Ni_{0.25}O_{2-\delta}$, compared with the reference compounds (JCPDF file 4-593 for CeO_2, 4-835 for NiO and 4-850 for Ni) where (*) denotes the reflections of La_2NiO_4 phase. In the inlet the magnification of the region $36° < 2\theta < 45°$ was reported.

2.3. Characterizations of catalysts

X-Ray diffraction patterns were measured by an X-ray diffractometer (Philips X-Pert 3710) using a CuKα radiation (λ = 1.5406 Å) operating on a continuous scan mode at 40 kV and 30 mA. The X-ray diffraction patterns were recorded in the scan ranges of $2\theta = 20°–75°$ at a scan rate of 1.5°/min. The main crystallites size of the revealed phases was calculated from the Scherrer equation, where the particle shape factor was taken as 0.9.

Temperature-programmed reduction (TPR) measurements were performed in a flow system at Micromeritics 2750 instrument, equipped with a TCD detector. In order to remove surface contaminants, the samples were preheated at 400 °C in an Argon stream for 1 h. After cooling at room temperature, a mixture of 50% H_2/Ar (30 cm^3/min) was flowed into the system and the temperature was raised up to 950 °C with a rate of 20 °C/min. The H_2 consumption was evaluated from integrating peak areas by comparison with those obtained by using CuO as a standard. The same instrument has been employed to measure the BET surface areas of the samples by nitrogen adsorption at liquid nitrogen temperature. Similarly, TPH of the spent catalysts, was performed in the same apparatus as described for H_2-TPR and the analysis process was identical to the H_2-TPR.

The structure and morphology of fresh catalysts were investigated by transmission electron microscopy (TEM) using a Philips CM12 instrument. Specimens were prepared by ultrasonic dispersion of the catalysts in isopropyl alcohol by depositing a drop of suspension on a holey copper grid. Mean nickel particle size, evaluated as the surface-area weighted diameter ($\bar{d}_s$), was derived according to:

$$\bar{d}_s = \frac{\sum_i n_i d_i^3}{n_i d_i^2}$$

The SEM–EDX investigations have been carried out with a FEI XL 30 microscope equipped with a field emission gun and EDX probe, operating at an accelerating voltage of 20 kV.

X-ray photoelectron spectra of the sample powders were recorded on a PHI Spectrometer (model 5800-01) equipped with an electron flood gun neutralizer and a monochromatic AlKα-source operating a 350 W. The X-ray photoelectron spectra were obtained with constant pass energy of 11.75 eV. Before spectral acquisitions, samples were out-gassed overnight in the preparation chamber of the spectrometer. The characteristic photoemission peaks from O(1s), C(1s), Ni(3p), La(3d) and Ce(3d) core levels were recorded for each samples. Binding energy was referenced to C 1s of adventitious carbon at 284.8 eV. Peaks fitting involved a deconvolution with the use of mixed Gaussian–Lorentian or Gaussian (for Ni 3p) functions. Both peaks fitting and chemical analysis, as chemical composition, were carried out by using the PHI Multipak v.6 software.

Elemental analysis, to detect the carbon deposition on the worked catalysts, was carried out with a Carlo Erba CHNS analyzer (mod. EA 1108).

3. Results and discussion

3.1. Characterization of catalysts

3.1.1. X-ray diffraction (XRD)

Fig. 1 shows the XRD patterns of the as prepared catalysts; in all samples the main reflections of CeO_2 can be evidenced suggesting that pure fcc fluorite structure is retained also at high lanthana content. Scarcely visible reflections due to NiO can be observed in the sample at low nickel content ($Ce_{0.70}La_{0.20}Ni_{0.10}O_{2-\delta}$), as envisaged in the inset of Fig. 1 that shows a magnification of the diffraction zone covering the reflections of Ni compounds. Increasing the nickel content, co-presence of metallic phase and additional La_2NiO_4 phase in the $Ce_{0.25}La_{0.50}Ni_{0.25}O_{2-\delta}$ sample, as results by

the appearance of the most intense diffraction line at $2\theta = 32.48^{\circ}$, emerges.

The CeO_2 peaks intensities decrease noticeably by increasing the La content, with an evident peaks shift toward lower angles which is also reflected by an increase in the lattice parameter "*a*", as reported in Table 1. The absence of La_2O_3 reflections, coupled with the poor detectability of Ni species, can support a partial substitution of La^{3+} and Ni^{2+} ions in the ceria lattice to form a complex solid solution, as previously observed [29], and tentatively formulated as $Ce_{1-3x}La_{2x}Ni_xO_{2-\delta}$. However, the formation of isolated La_2O_3 crystallites, too small to be detected by XRD, may not be excluded. The deformation of the CeO_2 structure, due to a partial replacement of Ce^{4+} ions (ionic radius = 0.097 nm) with La^{3+} (0.116 nm) and Ni^{2+} (0.081 nm), results in a lattice expansion that increases from 0.5% to 3.6% by increasing the La content, suggesting that oxygen vacancies have been formed intrinsically as stable form of non-stoichiometric oxides. This lattice expansion results in good agreement with previous literature related to the Ce—La—O system [31,32]. Theoretical investigations on mixed $Ce_{1-x}La_xO_{2-x/2}$ oxides, reported by Wilkes et al. [33] have highlighted the partial solubility of CeO_2 and lanthanum oxide. The authors have observed that, at low ionic fraction of lanthanum (*x*, ranging between $0 < x < 0.5$), lanthanum dissolved in ceria with lanthanum segregation on its surface occurs; while, at high lanthanum content ($x > 0.9$) cerium dissolved in lanthanum with ceria segregation can be predicted [34]. In the current samples, the molecular level mixing of the reactants, occurred during the combustion synthesis, can promote the solution solid formation even at high lanthanum concentration ($Ce_{0.25}La_{0.50}Ni_{0.25}O_{2-\delta}$); while the presence of nickel species on the sample surface can suggest a progressive phase segregation that becomes more severe by increasing the Ni amount [35].

The BET surface area of the catalysts, included in Table 1, increases slightly with the increase of the La content, confirming that the incorporation of trivalent dopant into CeO_2 can greatly promote the dispersion of oxides. The relatively low surface area of the samples is reasonable, considering that during the combustion synthesis temperature of ca. 1000 °C can be reached [36].

3.1.2. TEM and SEM–EDX analysis

TEM images of catalysts, pre-reduced at 450 °C, are shown in Fig. 2, we can observe that the average size of Ni particles increases from 5.7 nm to 9.8 nm by increasing the nickel content, as evidenced in Table 1. The low contrast between Ni and Ce—La—O support can confirm that part of nickel could be in spinel type oxides.

Besides, the "as prepared" samples have been tested by SEM–EDX in order to derive informations about micro-structural properties and nickel dispersion; the results are reported in Fig. 3 that includes for each sample the bright area image, the corresponding EDX map of Ni + La and the EDX spectrum. EDX mapping of the $Ce_{0.70}La_{0.20}Ni_{0.10}O_{2-\delta}$ sample (Fig. 3b) illustrates a uniform distribution of Ni + La in the near-surface region; further increase of the Ni content (Fig. 3c and b) leads to the increase in the related peak as well as the dot intensity of nickel, suggesting an agglomeration of the particles. Similar evidences can be derived for the La distribution, the derived La/Ni atomic ratio increases progressively by increasing the Ni content, reaching the nominal value (La/Ni = 2) only at the higher Ni content. As TEM analysis have highlighted a progressive increase in the Ni particle size by increasing the metallic load, whereby, it is reasonable suppose a progressive coverage of Ni particles by LaO_x species, as confirmed by the presence of La_2NiO_4 phase (revealed by X-ray diffraction) at high nickel content.

3.1.3. Temperature programmed reduction (TPR)

Fig. 4 shows the TPR profiles of the catalysts compared with a reference CeO_2 prepared by the same procedure; three reduction

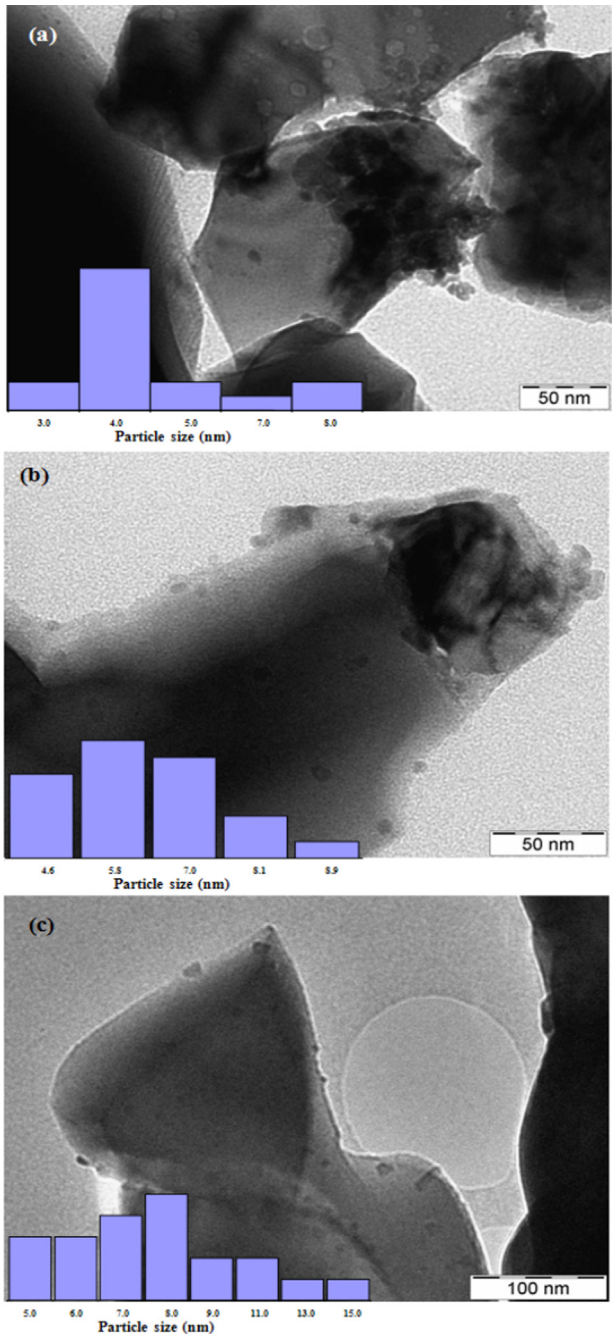

Fig. 2. TEM images of pre-reduced catalysts. (a) $Ce_{0.70}La_{0.20}Ni_{0.10}O_{2-\delta}$; (b) $Ce_{0.40}La_{0.40}Ni_{0.20}O_{2-\delta}$; (c) $Ce_{0.25}La_{0.50}Ni_{0.25}O_{2-\delta}$.

regions can be evidenced: (a) a low temperature region centered from 100 to 250 °C (denoted by α peak); (b) a region at intermediate temperature, where two reduction peaks can be envisaged and centered at 320 °C (β peak) and 420 °C (γ), respectively; (c) a high temperature region where the occurrence of two reduction peaks (δ′ and δ) can be displayed. The α peak is generally ascribed to the reduction of adsorbed oxygen on ceria surface, resulted from incorporation of La^{3+} and Ni^{2+} ions into ceria lattice. It is widely accepted that in the metal–ceria solid solutions, the incorporation of metal with lower valence into ceria lattice, to replace some Ce^{4+} cations, induces the unbalance of charge and the lattice distortion within the ceria structure with the generation of active oxygen vacancies leading to the formation of active oxygen species easily reducible by H_2 at low temperature [37]. Besides, the reduction of interfacial

Table 1
Physical properties of Ni/Ce—La—O mixed oxides.

Sample	Ni (wt%)	Surface area (m^2/g)	2θ (d_{111}) (degree)	a (nm)	CeO_2[a] (nm)	Ni[b] (nm)
$Ce_{0.70}La_{0.20}Ni_{0.10}O_{2-\delta}$	3.66	1.8	28.38	0.544	25.2	5.7
$Ce_{0.40}La_{0.40}Ni_{0.20}O_{2-\delta}$	7.88	2.9	27.87	0.552	26.9	6.8
$Ce_{0.25}La_{0.50}Ni_{0.25}O_{2-\delta}$	10.25	3.8	27.53	0.560	18.3	9.8

Note: α, unit cell parameter, calculated assuming a cubic system for the Ce—La—O mixed oxides.
[a] Particle size of cubic CeO_2, estimated according to the Scherrer equation applied to (1 1 1) reflection.
[b] Particle size of Ni, derived from TEM analysis.

Table 2
H_2 uptake (ml) during TPR experiments with the Ni/Ce—La—O samples.

Sample	H_2 uptake (ml)					H_2/Ni
	α	β	γ	δ'	δ	
$Ce_{0.70}La_{0.20}Ni_{0.10}O_{2-\delta}$	0.03	0.08	0.42		0.97	0.70
$Ce_{0.40}La_{0.40}Ni_{0.20}O_{2-\delta}$	0.10	0.19	0.19	0.14	0.27	0.59
$Ce_{0.25}La_{0.50}Ni_{0.25}O_{2-\delta}$	0.04	0.38	0.12	0.17	0.35	0.57

oxygen ions of the metal oxide species having interaction with the surface oxygen vacancies (IMOSI effect) [38,39] can contribute further to the H_2 consumption revealed by α peak. The related H_2 uptake (summarized in Table 2) increases noticeable by increasing the La content in the samples, at high level of doping a substantial decrease can be observed. The decline of the H_2 consumption at high level of doping can be due to the decrease in oxygen vacancies of ceria, for increasing amount of lanthanum the quantities of ceria and hence its surface oxygen vacancies become increasingly fever as La^{3+} content is increased. Besides, co-doping ceria with lower valence metal oxide leads to the introduction of oxygen vacancies that can be expressed by Kröger–Vink notation as:

$$La_2O_3 \xrightarrow{2CeO_2} 2La'_{Ce} + 3O_O{}^{x} + V_O{}^{\bullet\bullet}$$

$$NiO \xrightarrow{CeO_2} Ni''_{Ce} + O_O{}^{x} + V_O{}^{\bullet\bullet}$$

where La'_{Ce} and Ni''_{Ce} represent one Ce^{4+} site occupied by La^{3+} and Ni^{2+} ions, respectively. The addition of La_2O_3 and NiO into CeO_2 system would lead to the formation of more oxygen vacancies due to the charge compensation in the material; the vacancies ($V_O{}^{\bullet\bullet}$) with positive charge may attract the doping ions (La'_{Ce} and Ni''_{Ce}) with negative charge to produce complexes ($2La'_{Ce}V''_O/2La'_{Ce}V''_O La'$ and $Ni''_{Ce}V''_O/Ni''_{Ce}V''_O Ni''_{Ce}$) due to electrostatic attractions, in accordance with as reported by Zhang et al. [40]. At low dopant concentration most of the oxygen vacancies $V_O{}^{\bullet\bullet}$ are probably free and mobile while at high level of doping, the defects association near the dopants begin to form, this trapped vacancies can limit the CeO_2 reducibility. [41].

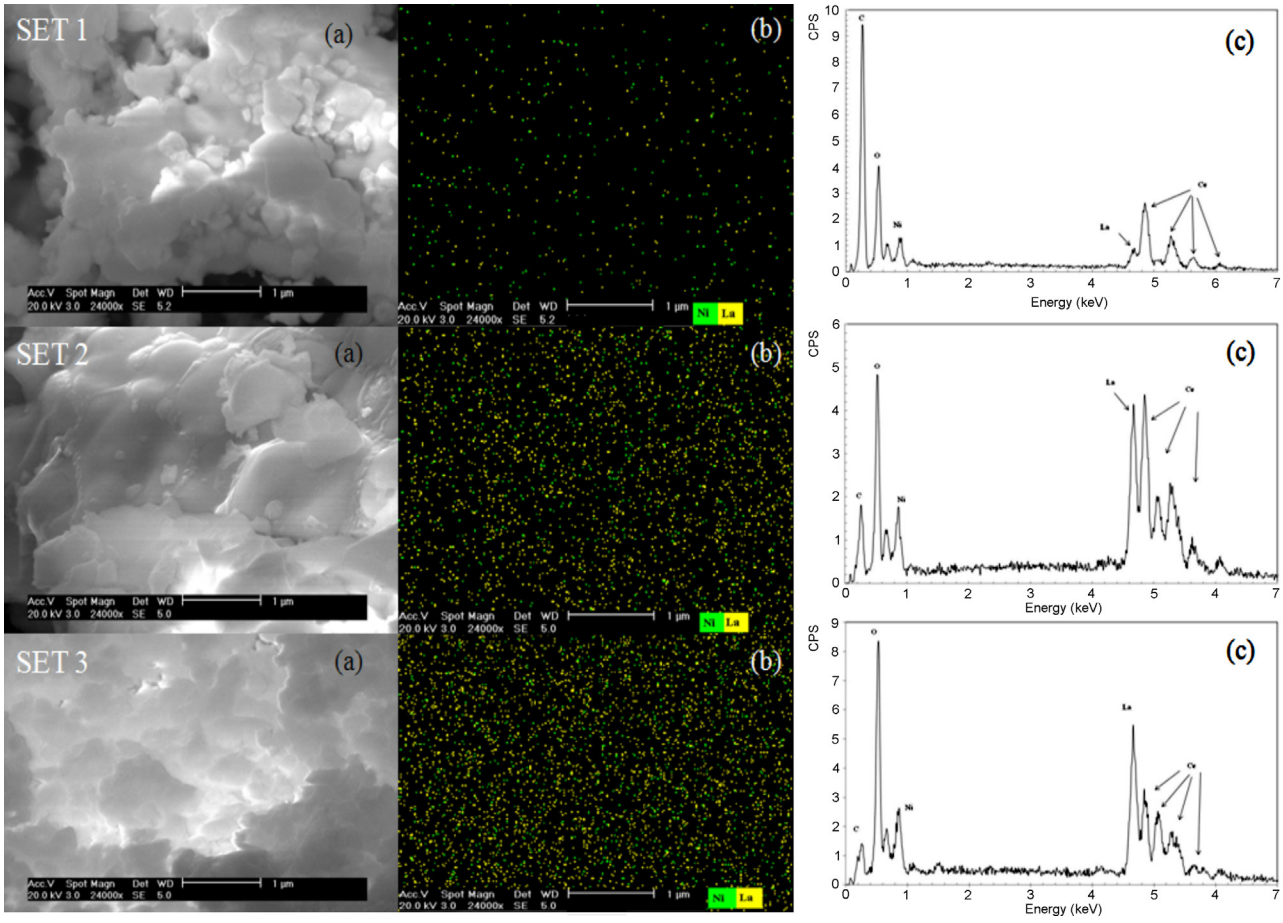

Fig. 3. SEM images (a), Ni + La mapping (b), EDX spectrum (c) of the different catalysts: SET 1 ($Ce_{0.70}La_{0.20}Ni_{0.10}O_{2-\delta}$); SET 2 ($Ce_{0.40}La_{0.40}Ni_{0.20}O_{2-\delta}$); SET 3 ($Ce_{0.25}La_{0.50}Ni_{0.25}O_{2-\delta}$).

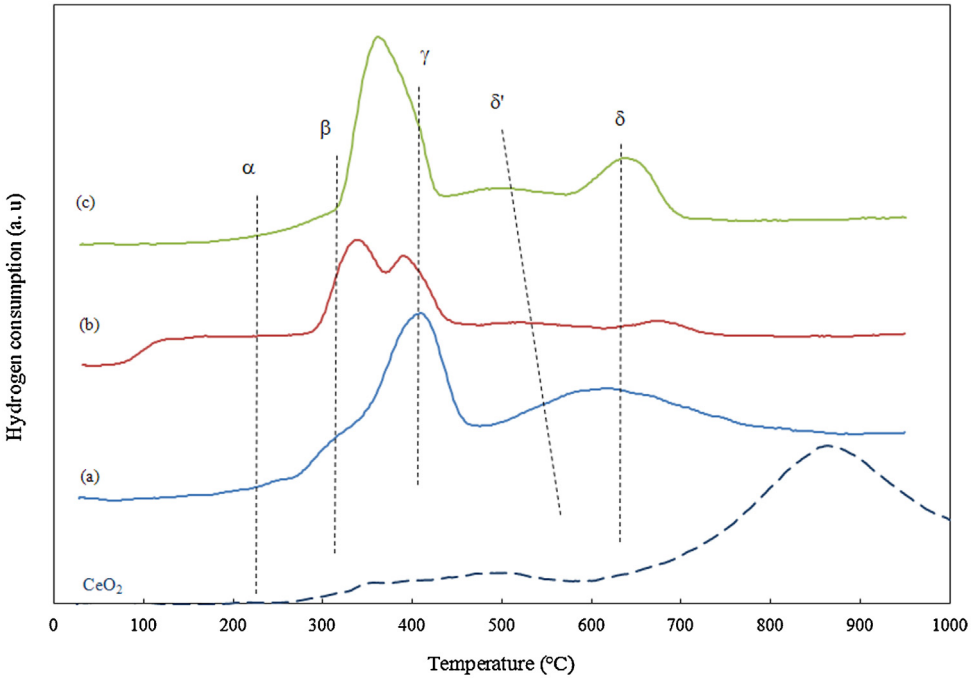

Fig. 4. H_2 consumption profiles during TPR of the catalysts: (a) $Ce_{0.70}La_{0.20}Ni_{0.10}O_{2-\delta}$; (b) $Ce_{0.40}La_{0.40}Ni_{0.20}O_{2-\delta}$; (c) $Ce_{0.25}La_{0.50}Ni_{0.25}O_{2-\delta}$, compared with CeO_2 sample.

Increasing the Ni content the β peak shifts to high temperature, its intensity increases while a proportionally decrease of γ peak (that become a shoulder of β peak at high Ni load, $Ce_{0.25}La_{0.50}Ni_{0.25}O_{2-\delta}$ sample) is observed. The β and γ peaks are generally due to the stepwise reduction of NiO species; β peak corresponds to the reduction of aggregated NiO dispersed on surface with small interactions with the support; while γ peak is attributable to crystalline bulk-like nickel phase strongly interacting with ceria–lanthana support [42]. The shift of β-peak toward higher reduction temperature implies an increase in Ni^{2+}-support interactions, induced by lanthana (La/Ni = 2), while the CeO_2 content proportionally decreases; this determines a decrease in the number of interactions between nickel species in the nickel–cerium solid solution and/or at the interface between NiO grains and ceria. As consequence, a proportional increase in the NiO aggregates relatively free on the surface at the expense of NiO species with stronger interaction with support occurs. The increasing presence of large nickel aggregates implies that the dispersion of nickel species becomes poorer with increased loading, in accordance with TEM analysis that reveals a progressive increase in the Ni particle size (Table 1) and by SEM–EDX evidences. These results suggest the existence of strong metal–support interaction (SMSI) between NiO and La—Ce—O support while the Ni—Ce interactions decrease by increasing the nickel content.

The bulk CeO_2 reduction peak (δ) appears similarly influenced by lanthanum introduction; surface and bulk ceria reduction, evidenced at about 450 and 860 °C respectively, becomes indiscernible in the $Ce_{0.70}La_{0.20}Ni_{0.10}O_{2-\delta}$ sample, with the occurrence of a single peaks centered at 620 °C. Increasing the La content, the presence of a new reduction peak (δ′) at lower temperature (500 °C) can confirm a higher Ce^{4+} replacement by La^{3+} and Ni^{2+} ions that promotes the diffusion of O^{2-} anion within the lattice, facilitating the bulk and surface reduction at lower temperature. Parallel, the δ peak relatively shift to high temperature, stepwise decomposition of hydroxyl-carbonates $La_2(OH)_4(CO_3)$, formed by air exposition of the samples, to $La_2O_2CO_3$ at about 500 °C, and further to La_2O_3 (occurring between 600 and 800 °C) can be responsible of the observed reduction profiles [43]; likewise the La_2NiO_4 reduction, revealed by XR diffraction in the $Ce_{0.25}La_{0.50}Ni_{0.25}O_{2-\delta}$ sample, that requires a temperature higher than 680 °C for its complete reduction, can be responsible of the observed behavior [44]. Besides, at high La/Ce atomic ratio, the electron-transfer process (La ← O) due to the more electronegative La^{3+} ions surrounding Ce^{4+}, can hinder the reduction process that occurs at higher temperature [45].

Finally, the derived H_2/Ni ratio (Table 2), results lower than the theoretical value of unit suggesting that NiO in all catalysts is not completely reduced, the reduction degree decreases with the rise of nickel loading, thus it is very likely that some NiO can be incorporated in the mixed oxides and consequently more difficult to reduce so the reduction peaks do not appear in TPR profile [46]. Besides the progressive increase in the lantana content, by increasing the Ni load, can hinder the reduction due to a blocking effect of nickel crystallites by species originating from the support (e.g. LaO_x species).

3.1.4. XPS surface analysis

The surface characteristics of the pre-reduced samples were examined by XPS. The relevant atomic ratios as well the binding energies, determined from the fitting for the main peaks in O 1s, Ni 3p and La $3d_{5/2}$ core levels regions are described in Table 3.

The O 1s profile is rater complex as judging from the tree component derived from the fitting, these peaks appear at: (a) 528.3–528.8 eV; (b) 529.0–531.5 eV; (c) 531.5–532.4 eV, respectively. The type (a) peak is usually ascribed to lattice oxygen (O^{2-}) whereas (b) and (c) type components generally arise from hydroxyl and carbonate groups (~531.6 eV) and well as adsorbed water (~533.2 eV [47]). However, as evidenced in Table 3, the binding energies (BE) for all peaks appear lower than the reference values; particularly the BE of O 1s for Ce^{4+}—O^{2-} system, generally observed at 529.6 eV [48], appears shifted to lower BE, this negative shift results more pronounced with the sample at low Ni and La content. Similar results have been evidenced by Reddy et al. [49] with $Ce_{1-x}La_xO_{2-\delta}$ solid solutions, the Authors have highlighted a chemical shift of −1.0 eV ascribed to the basic nature of La^{3+} that can push the electron density toward oxide ion. The progressive shift to lower binding energy, by decreasing the Ni content in the

Table 3
Data from XPS analysis of pre-reduced catalysts.

Sample	Binding energy (eV)				Surface composition (at%)			Ce^{4+} (at%)		Ce^{3+} (at%)	
	Ni $3p^a_{3/2}$	Ni $3p^b_{3/2}$	O 1s	La $3d_{5/2}$	Ni 3p	La 3d	Ce 3d	In Ce	On surface	In Ce	On surface
$Ce_{0.70}La_{0.20}Ni_{0.10}O_{2-\delta}$	65.5(1.36)[b]	68.9	528.3(22)[a] 529.2(34)[a] 532.1(43)	833.51	1.4	3.0	9.1	54	4.9	46	4.2
$Ce_{0.40}La_{0.40}Ni_{0.20}O_{2-\delta}$	65.6(1.42)[b]	68.8	528.7(47)[a] 529.0(16)[a] 531.5(36)[a]	833.62	3.7	8.1	6.8	53	4.8	47	4.3
$Ce_{0.25}La_{0.50}Ni_{0.25}O_{2-\delta}$	66.0(0.78)[b]	68.6	528.8(59)[a] 531.5(37)[a] 532.4(4)[a]	834.00	3.7	10.2	5.1	50	4.5	50	4.5

[a] Numbers in parentheses are the peak percentage.
[b] Values in parentheses are the area ratios corresponding to Ni $3p^a_{3/2}$ peak and Ni $3p^b_{3/2}$ peak.

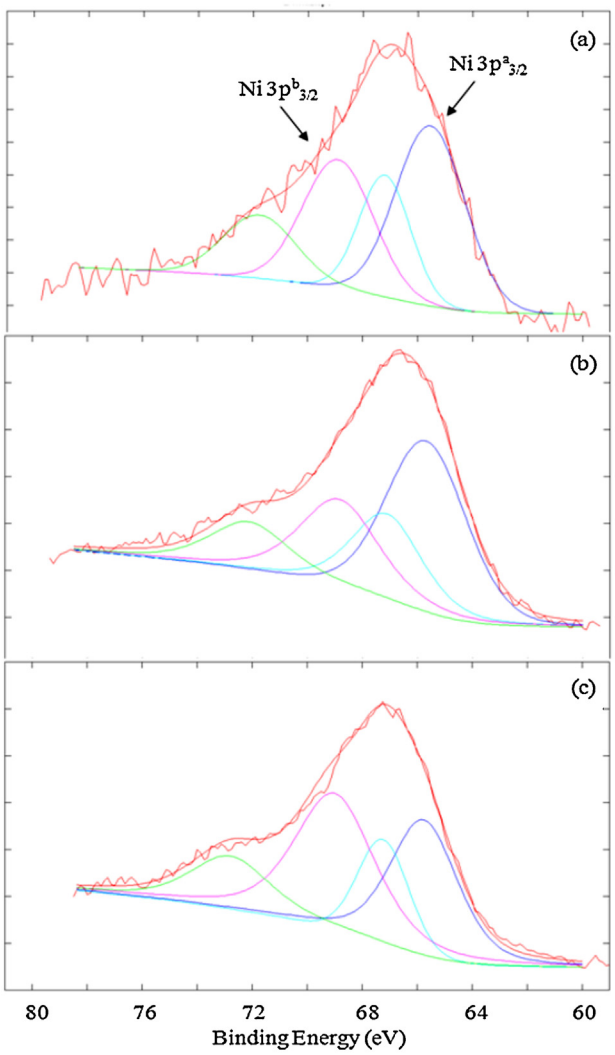

Fig. 5. Ni 3p XPS spectra of pre-reduced catalysts: (a) $Ce_{0.70}La_{0.20}Ni_{0.10}O_{2-\delta}$; (b) $Ce_{0.40}La_{0.40}Ni_{0.20}O_{2-\delta}$; (c) $Ce_{0.25}La_{0.50}Ni_{0.25}O_{2-\delta}$.

samples, can indicate a higher electron acceptance capacity and thus a higher basicity that increases by decreasing the Ni and La content in the samples [50].

Fig. 5 shows the Ni 3p XPS spectra of the studied samples. The Ni 2p signal, generally used for analytical purposes, results very complex due to overlapping of Ni $2p_{3/2}$ and La $3d_{5/2}$ peaks, so that it may influence not only the accurate measure of the BE of nickel but also its intensity [47]. In order to overcome this difficulty, the Ni 3p spectrum has been evaluated considering the Ni $3p_{3/2}$ and Ni $3p_{1/2}$ contributions; while, the satellites at about 7 eV and 13 eV from the Ni $3p_{3/2}$ line were not included because they hinder the separation between the Ni $3p_{3/2}$, $p_{1/2}$ doublets, in accordance with as reported by Gorgoi et al. [51]. The large value of the FWHM (full with half maximum) of Ni 3p peak and its asymmetry on the high binding energy side suggests that the Ni $3p_{3/2}$ peak, as well as the Ni $3p_{1/2}$, might consist of more than one contribution. Thus both lines were deconvoluted to two peaks (Ni $3p^a_{3/2}$ and Ni $3p^b_{3/2}$) with the least-squares fitting routine using a Gauss function, the results are depicted in Fig. 5 and synthesized in Table 3. The Ni $3p^a_{3/2}$ peak located at 65.5–66.0 eV can be assigned to metallic nickel; while the Ni $3p^b_{3/2}$ component, centered at 68.9–68.6 eV, can be attributed to Ni^{2+} species. The BE value of metallic nickel appears lower than the reference values (66.2 eV [52,53]) suggesting an electron interaction between nickel species and support, that

increases by decreasing the Ni—La content in the samples and associated with the decrease in surface segregation of La. At the same time, a decrease in the BE of La $3d_{5/2}$ (Table 3) is observed; the reported reference value for La^{3+} (La_2O_3) is 834.8 eV [54], the progressive shift to lower values may imply the partially reduction of La_2O_3 to LaO_x ($x<3$) during the pre-reduction step of the catalysts. LaO_x species act as an electron donor that can transfer partial electrons to Ni, resulting in an increase in d-electron density of the surface Ni atoms, as a consequence the binding energy of Ni 3p over the catalyst shifts to lower value [55]. This effect appears strictly related to the La^{3+} content on the surface, at low load the high dispersion can promote the electron-donor effect while at high loads the aggregation or the formation of isolated La_2O_3 crystallites (or La_2NiO_4) can hinder this effect. The phenomena of electron transfer between other metals and Ni has been shown in different catalytic systems, a significant electron transfer from Sr to Ni in Sr-doped Ni-La_2O_3 catalysts has been evidenced by Sutthiumporn et al. [56], as well as in other catalysts such as Au–Ni/Al_2O_3 [57] and Ni-doped titanium [58].

Moreover, the BE value of Ni^{2+} is higher than that usually reported for NiO (68.0 eV [59]) suggesting the presence of Ni^{2+} species with a more high cationic character than in NiO. Species with highly cationic character could be formed by SMSI effect.

BE values of Pd $3d_{5/2}$ significantly higher than reported for PtO were observed by Borchert et al. [60] in a study related to Pd/$Ce_{1-x}Ga_xO_{2-y}$ samples. This evidence was ascribed by the authors to the presence of Pd^{2+} ions with a more cationic character than in PtO, formed by strong metal support interactions, where the Pd—O bonding belonged to Pd—O—Ce or Pd—O—Gd configurations at the Pd/support interface. Analogous effect has been evidenced in the La-doped Pd/CeO_2 catalysts [61]; the observed more cationic $Pd^{\delta+}$ state, resulting from a closer contact between support and metal or SMSI effect, was ascribed to the high oxygen mobility due to the lanthana introduction into CeO_2 lattice that could facilitate the reduction of CeO_2 and maintain the Pd in a more cationic state.

In the current catalysts, the BE shift of the Ni $3p^b{}_{3/2}$ peak becomes more positive by decreasing the Ni—La amount, a progressive increase in the interactions between Ni ions and support with formation of Ni—O—La or Ni—O—Ce bonds can be assumed. A steady decrease in the Ni^0/Ni^{2+} ratio (corresponding to the peak area ratio, as reported in Table 3) implies a progressive decrease in the contribution of Ni^0 phase from 58 to 57% with the $Ce_{0.70}La_{0.20}Ni_{0.10}O_{2-\delta}$ and $Ce_{0.40}La_{0.40}Ni_{0.20}O_{2-\delta}$ samples, and a noticeable decrease to 44% of the sites on the surface after the pre-reduction process, at high nickel content. All this results confirm the TPR evidences.

Ce 3d XPS spectra of the reduced catalysts are shown in Fig. 6. As widely reported in literature [62,63], both Ce $3d_{5/2}$ and Ce $3d_{3/2}$ levels present five component v_o, v, v', v'', v''' and u_o, u, u', u'', u''', respectively. As the insertion of La^{3+} and Ni^{2+} ions in the ceria lattice can increase the formation of Ce^{3+} species, the XPS spectra of the $Ce_{1-3x}La_{2x}Ni_xO_{2-\delta}$ catalysts were studied in order to estimate the contribution of Ce^{4+} and Ce^{3+}. Since the features characteristic of the Ce^{3+} states derives from the contribution of u_o, v_o, v' and u', the following equation was used to estimate the cerium oxide stoichiometry:

$$Ce^{3+}(\%) = \frac{u_o + v_o + v' + u'}{\sum(u+v)}$$

referred to all states [64], using this method the fitted peak areas in the XPS spectra were employed. As evidenced in Table 3, the relative concentration of Ce^{3+} increases with the increase of lanthana content indicating that its presence facilitates the reduction of the cerium surface species, as evidenced by TPR analysis. Besides, the difference between the surface content of Ce^{3+} appears substantial invariant in all samples, thus it is probable that the oxygen vacancies rather than the abundance of Ce^{3+} have an influence on the catalytic activity.

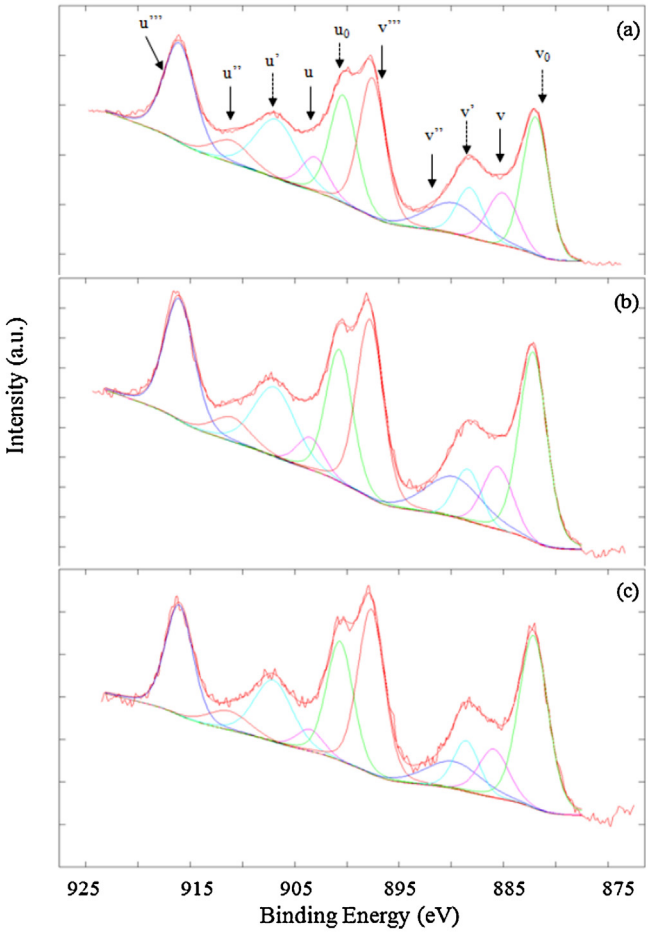

Fig. 6. Ce 3d XPS spectra of pre-reduced catalysts: (a) $Ce_{0.70}La_{0.20}Ni_{0.10}O_{2-\delta}$; (b) $Ce_{0.40}La_{0.40}Ni_{0.20}O_{2-\delta}$; (c) $Ce_{0.25}La_{0.50}Ni_{0.25}O_{2-\delta}$.

3.2. Catalytic activity tests

3.2.1. Effect of inlet O_2

The effect of different O_2 concentrations in the tri-reforming reaction, with the studied catalysts under a molar ratio in the feed of CH_4:CO_2:H_2O = 1:0.46:0.46, is given in Fig. 7. The catalyst at lower Ni content ($Ce_{0.70}La_{0.20}Ni_{0.10}O_{2-\delta}$) shows a CH_4 conversion rate of 1.77 mmol/s g_{Ni} (X_{CH_4} = 94%) at O_2/CH_4 = 0.05 that progressively reaches 1.82 mmol/s g_{Ni} (X_{CH_4} = 97%) by increasing the O_2 concentration. Parallel, a decrease in the CO_2 conversion rate, more evident at high oxygen content in the reaction's stream (O_2/CH_4 = 0.10), is observed. This evidence confirms that the added oxygen promotes the CH_4 conversion but has a contrary effect on the CO_2 conversion, since the CO_2 conversion is related to the CO_2 produced by combustion of methane and to the CO_2 consumed by reforming reaction. The H_2/CO molar ratio (not showed) increases from 1.60 to 1.64 by increasing the O_2/CH_4 ratio, strictly related the methane conversion. The methane and carbon dioxide conversions, at all the investigated O_2/CH_4 ratios, result slight higher than the predicted equilibrium values (reported in Table 4) while the measured H_2/CO molar ratios are slightly lower. This evidence suggests that other reactions are taking place, like methane decomposition (Eq. (4)), occurring in feeds containing high CH_4/CO_2 molar ratios and favored at high temperatures. The absence of deactivation phenomena during the experimental tests implies the gasification

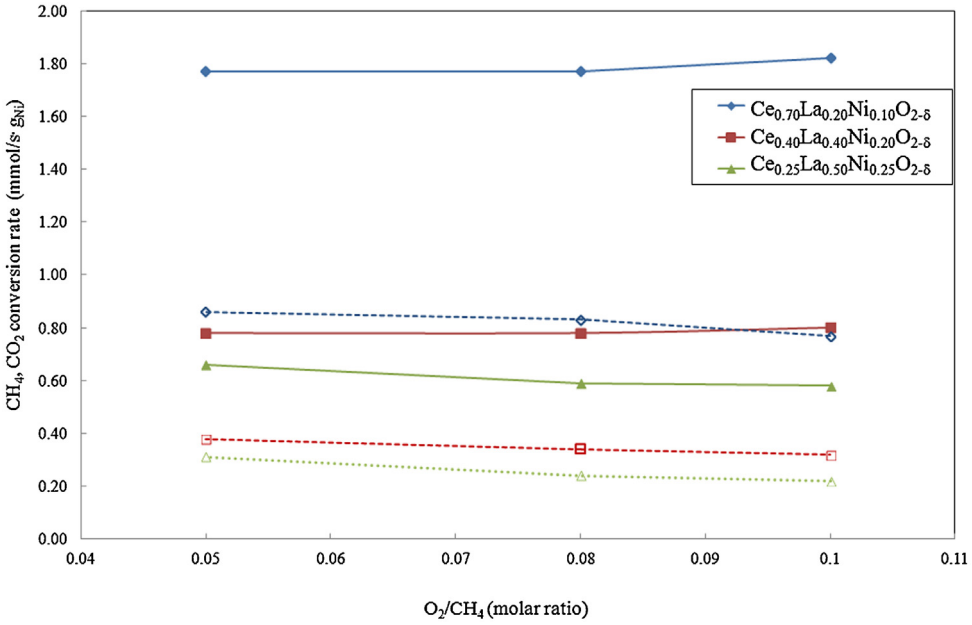

Fig. 7. Effect of O_2/CH_4 ratio on the performance of the different catalysts during tri-reforming reaction tested under a GHSV = 31,000 h^{-1}, T = 800 °C (filled symbols: CH_4 conversion rate; unfilled symbols: CO_2 conversion rate).

of the carbon deposits. In the CH_4–CO_2 reforming system carbon is also produced by the following reactions: $2CO \leftrightarrow CO_2 + C$ and $CO + H_2 \leftrightarrow C + H_2O$, that are un-favored at high temperatures, as consequence its irreversibility may facilitate the carbon removal process through gasification of coke. Besides, the high CO_2 conversion can be due to the contribution of reverse water gas shift reaction (RWGS: $CO_2 + H_2 \leftrightarrow CO + H_2O$). The experimental steam conversion (not shown) and the H_2/CO ratio lower than the theoretical can confirm this hypothesis. Moreover, the moderate basicity of the catalysts, induced by lanthana, can increase the selectivity of the catalysts for dry reforming reaction, that produces 1 mol H_2 less and 1 mol CO more per mole of reacted methane, than in the steam reforming reaction.

Analogous behavior is observed with $Ce_{0.40}La_{0.40}Ni_{0.20}O_{2-\delta}$ sample but the catalytic performance appears lower than previous one; a light increase in the H_2/CO molar ratio from 1.60 to 1.65 by increasing the O_2 added is observed. A further decrease in the catalyst's performance is observed with the $Ce_{0.25}La_{0.50}Ni_{0.25}O_{2-\delta}$ sample; CH_4 and CO_2 conversion rates decrease also by increasing the oxygen content in the reaction's stream. The derived H_2/CO ratio, compared with previous catalysts in the same conditions, increases to 1.62 at low O_2 content (O_2/CH_4 = 0.05) and increases progressively to 1.64 by further O_2 introduction. Besides, both samples at low Ni content ($Ce_{0.70}La_{0.20}Ni_{0.10}O_{2-\delta}$; $Ce_{0.40}La_{0.40}Ni_{0.20}O_{2-\delta}$) show a catalytic activity that remains constant along the time on stream and for all the investigated O_2/CH_4 molar ratios, as evidenced in Fig. 8a for a representative catalytic test carried out at a molar ratio O_2/CH_4 = 0.1.

Table 4
Biogas equilibrium conversion, calculated at 800 °C.

Gas composition (CH_4:CO_2:H_2O:O_2)	X_{CH_4}	X_{CO_2}	H_2/CO
(1:0.46:0.46:0.05)	90.78	90.37	1.66
(1:0.46:0.46:0.08)	93.02	87.18	1.67
(1:0.46:0.46:0.10)	94.17	84.75	1.67
(1:0.96:0.96:0.07)	99.23	53.88	1.53
(1:0.60:0.60:0.07)	97.12	75.39	1.63
(1:0.44:0.44:0.07)	90.88	90.06	1.67
(1:0.40:0.40:0.07)	86.95	93.09	1.68
(1:0.66:0.66:0.10)	98.20	67.18	1.61

The $Ce_{0.25}La_{0.50}Ni_{0.25}O_{2-\delta}$ sample instead shows a light deactivation, decreasing both the methane and the CO_2 conversion rates during the time on stream at all the investigated O_2/CH_4 molar ratios; a deactivation of 21% in the test at low oxygen content (O_2/CH_4 = 0.05) that decreases to 19% by increasing the O_2 in the feed, as depicted in Fig. 8b, is observed. The slight increase in the H_2/CO ratio, observed by increasing the Ni content in the catalysts at each investigated O_2/CH_4 molar ratio, can be related to the increases in the Ni particles size, evidenced by TEM and SEM–EDX investigations; larger metal particles favored the CH_4 cracking reaction that can, in turn, contribute to the increase of the H_2/CO ratio [8,65].

The carbon balance and pressure drop (measured along the catalytic bed) during the activity tests reported in Fig. 7, are used as preliminary indicators of the carbon deposition; a carbon balance of 100 ± 3% associated with an invariant pressure drop, recorded during every catalytic tests, can indicate that there was no significant carbon deposition during the time on stream and for all the catalysts. This apparent contradiction can be explained as follows.

Carbon deposition phenomena [66–68], metal sintering [69] and re-oxidation of the active phase are evidenced as the main causes for Ni-catalysts deactivation in reforming reactions. The apparent absence of carbon deposition, revealed during previous tests despite the high CH_4 concentration in the reactants stream, evidences that the reactions leading carbon deposition (Eqs. (4) and (5)) and those that can convert carbon (Eqs. (6)–(8)), favored by the presence of H_2O and O_2, can be kept in balance. It is widely accepted [70,71] that the methane dry reforming reaction proceeds via the dissociative adsorption of CH_4 on the Ni surface whereas the support can provides sites for CO_2 activation. CH_4 and/or O_2 dissociate rapidly on metallic Ni sites, while the presence of ceria enhances the water dissociation and transfer the produced oxygen to the supported metal, reducing the coke formation [72]. From the above analysis it is clear that over the Ni/La—Ce—O catalysts both metal and support play a very important role in reforming reactions.

The performance of the catalysts, decreasing in the order $Ce_{0.70}La_{0.20}Ni_{0.10}O_{2-\delta} > Ce_{0.40}La_{0.40}Ni_{0.20}O_{2-\delta} > Ce_{0.25}La_{0.50}Ni_{0.20}O_{2-\delta}$, appear at first closely related to the reducibility and particle size of nickel phase. It has been generally agreed that with oxygen-ion conducting support the catalytic activity is dependent, and

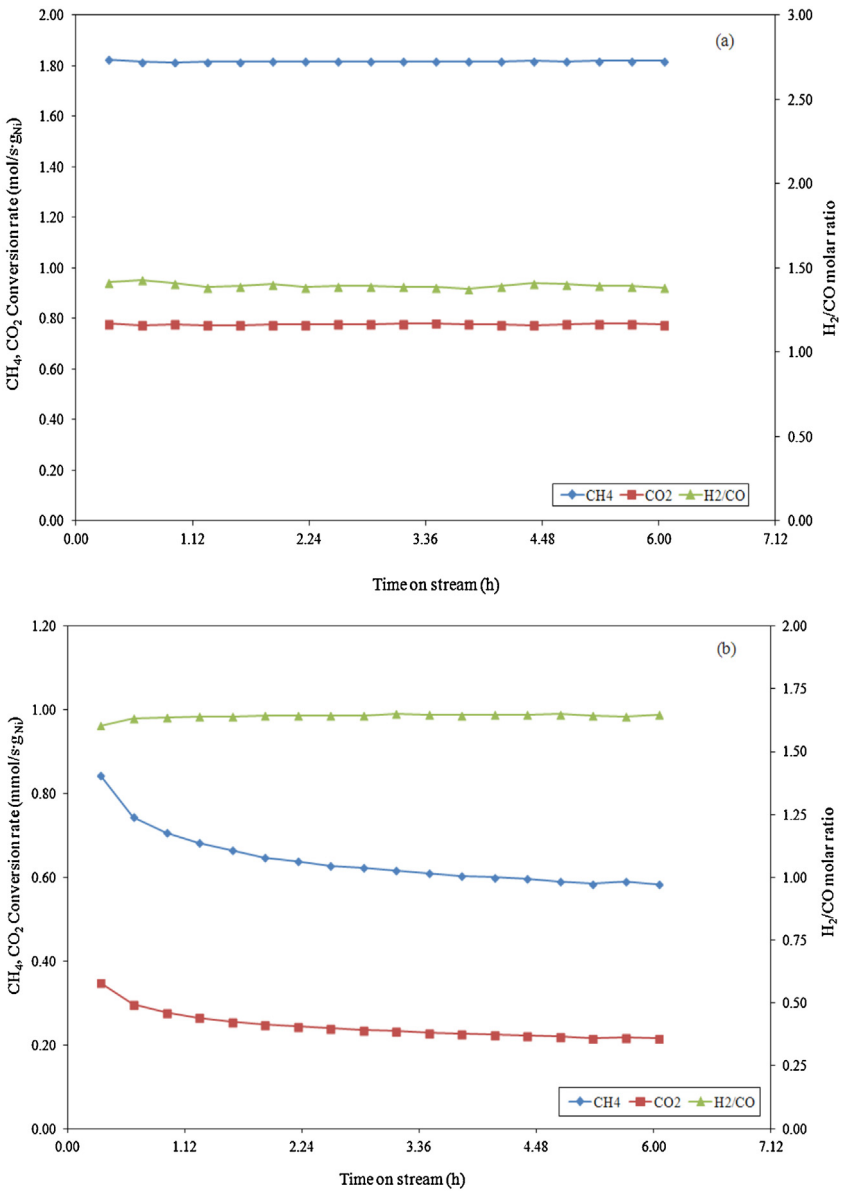

Fig. 8. CH_4, CO_2 conversion rates and H_2/CO ratio with time on stream over the more representative catalysts: (a) $Ce_{0.70}La_{0.20}Ni_{0.10}O_{2-\delta}$; (b) $Ce_{0.40}La_{0.40}Ni_{0.20}O_{2-\delta}$ samples.

controlled, by the number of the interfacial active centers which are related to the amount of metal oxide species having interaction with the surface oxygen and quantified by the TPR α-peak [38]. The H_2 consumption in α-peak increases progressively from $Ce_{0.70}La_{0.20}Ni_{0.10}O_{2-\delta}$ to $Ce_{0.40}La_{0.40}Ni_{0.20}O_{2-\delta}$ samples while the nickel particle size decrease, this implies that the active area of Ni available for CH_4 dissociation and the metal support-interfacial area decreases with loss of catalytic activity. In the $Ce_{0.25}La_{0.50}Ni_{0.20}O_{2-\delta}$ sample, the progressive increase in the amount of free NiO species (revealed by β peak in TPR analysis) and the low presence of interfacial sites can result in the nickel sintering during trireforming reaction.

XPS investigations have highlighted the presence of metallic nickel associated with cationic Ni^{2+} species on the catalyst's surface; as derived the d-electron density of the surface nickel atoms induced by LaO_x, species coupled with the Ni^{2+} species at high cationic character decrease in the same order of the catalytic activity:

$Ce_{0.70}La_{0.20}Ni_{0.10}O_{2-\delta} > Ce_{0.40}La_{0.40}Ni_{0.20}O_{2-\delta} > Ce_{0.25}La_{0.50}Ni_{0.25}O_{2-\delta}$

It is well know [54,73] that the increase in the d-electron density of the surface nickel atoms inhibit the electron donation from the HOMO of CH_4 to the lowest unfilled d orbitals of nickel atoms, whereby the activity of methane dehydrogenation to carbon deposits decreases. As consequence, the d-electron of nickel atoms can be donated to the vacant anti-bonding π^* orbit of the CO_2 molecules, this weakness the C—O bond, activating the CO_2. The activated CO_2 can react with the surface carbon, formed by methane dehydrogenation, forming CO; therefore the carbon elimination ability of CO_2 is promoted ($C + CO_2 \rightarrow 2CO$), this effect can contribute to minimize the carbon deposition.

Parallel, the Ni^{2+} species in electron-deficient state are able to accept σ electrons of C—H bond, promoting the cleavage of the bond enhancing the CH_4 conversion.

On this basis it is probable that the high electron density on metallic nickel associated with a high concentration of electron deficient Ni^{2+} species contributes to the observed catalytic activity.

The $Ce_{0.40}La_{0.40}Ni_{0.20}O_{2-\delta}$ sample has a larger amount of oxygen vacancies than the $Ce_{0.70}$ $La_{0.20}Ni_{0.10}O_{2-\delta}$ sample, but larger Ni particle size so, we can assume that, the amount of oxygen

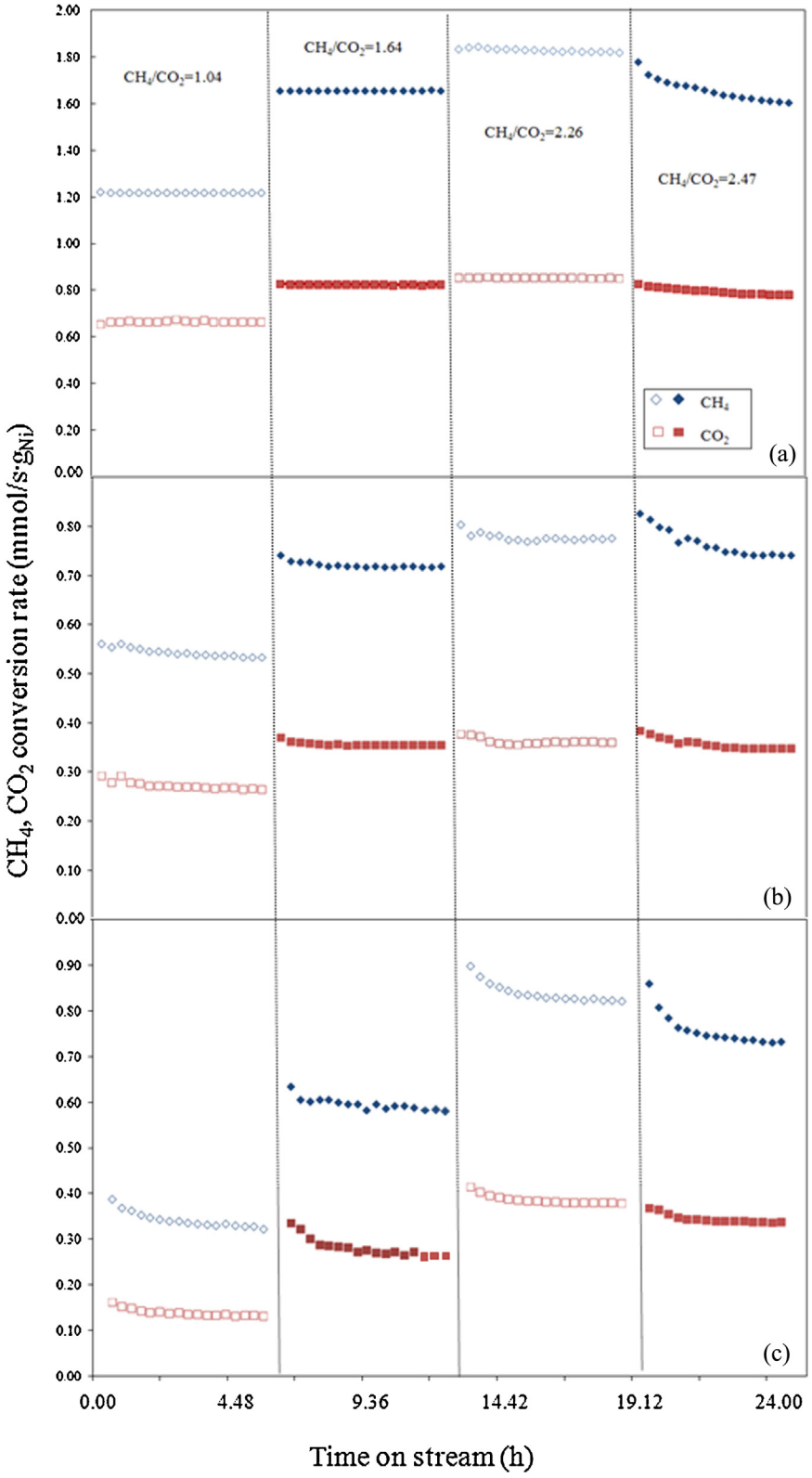

Fig. 9. Effect of CH_4/CO_2 molar ratio on the performance of the Ni/Ce–LaO catalysts in the tri-reforming reaction: (a) $Ce_{0.70}La_{0.20}Ni_{0.10}O_{2-\delta}$; (b) $Ce_{0.40}La_{0.40}Ni_{0.20}O_{2-\delta}$; (c) $Ce_{0.25}La_{0.50}Ni_{0.25}O_{2-\delta}$ samples.

available per metal–support interfacial area should be approximately the same on both catalysts. This activated oxygen species can activate the O_2 and H_2O molecules which can accelerate carbon removing, thus enhancing the activity and stability of the catalysts. While, the higher active area of metallic nickel, due to the lower particle size, associated with a higher electron density of the metal in $Ce_{0.70}La_{0.20}Ni_{0.10}O_{2-\delta}$ may favor the methane activation with an increase of the catalytic activity.

Besides, the surface defects of ceria are sites for oxygen adsorption; the chemisorbed oxygen, largely influenced by the presence

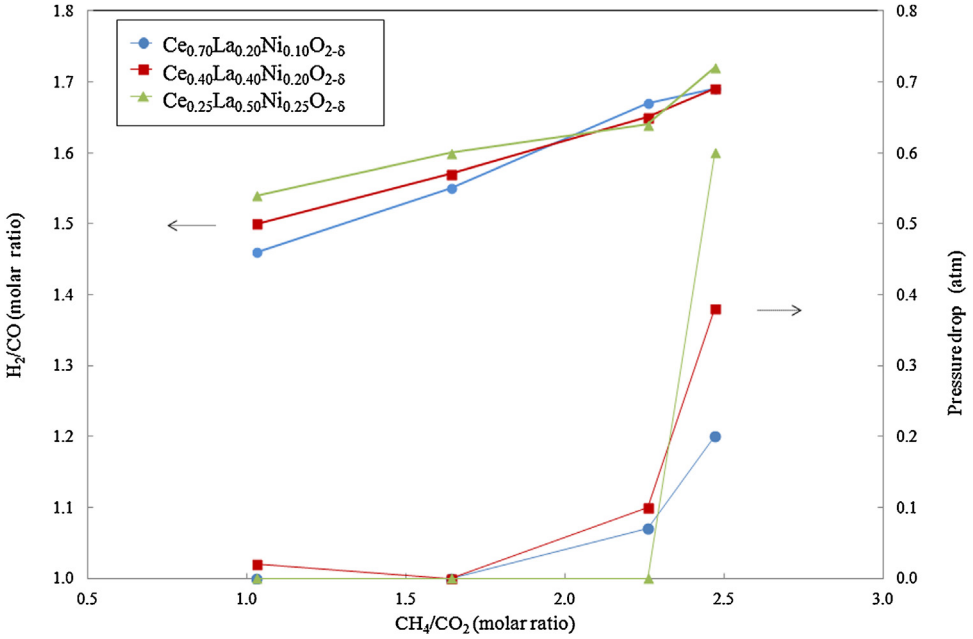

Fig. 10. Influence of CH_4/CO_2 molar ratio in the feed on the H_2/CO ratio in the reactions' products, compared with the observed pressure drop.

of oxygen vacancies, can evolve as lattice oxygen restoring the reduction of Ce^{4+} to Ce^{3+} ($2Ce^{3+} + ½O_2 + [*] \rightarrow 2Ce^{4+} + O_o{}^x$, where $O_o{}^x$ = oxygen in a normal site and [*] = anionic vacancies) [74]. In the current samples the increase in the nickel amount imply a decrease in the ceria content and then a decrease in the surface availability of oxygen vacancies, as evidenced by the almost constant Ce^{3+} content on the catalysts surface (from XPS analysis). The excess of oxygen not involved in the vacancies interactions can be able to oxidize both the deposited carbon and the Ni dispersed on the catalysts surface in weak interactions with the support (revealed by β peak in TPR analysis). This can cause the catalyst decay, observed with $Ce_{0.25}La_{0.50}Ni_{0.25}O_{2-\delta}$ sample, in absence of carbon deposition. Further, carbon dioxide can be easily adsorbed on support via the affinity of oxygen vacancies to the negative dipole of CO_2 coupled with a preferential adsorption on basic La_2O_3 or on the LaO_x species that can decorate the Ni crystallite [75]. The formed $La_2O_2CO_3$ and/or the formate species can in turn accelerate the conversion of surface CH_x species, coming from CH_4 dehydrogenation, accelerating the elimination of surface carbonaceous species. Similar to sulfur passivated reforming catalysts, the La_2O_3 partially can cover the catalyst in a way that the oxide blocks the Ni sites for nucleation of carbon [76]. The increasing amount of added La_2O_3, can in this way, reduce both catalytic activity and carbon deposition.

3.2.2. *Effect of inlet CH_4/CO_2 ratio*

The effect of CH_4/CO_2 molar ratio, has been evaluated under an initial feed composition of CH_4:CO_2:H_2O:O_2 = 1:0.96:0.96:0.07;

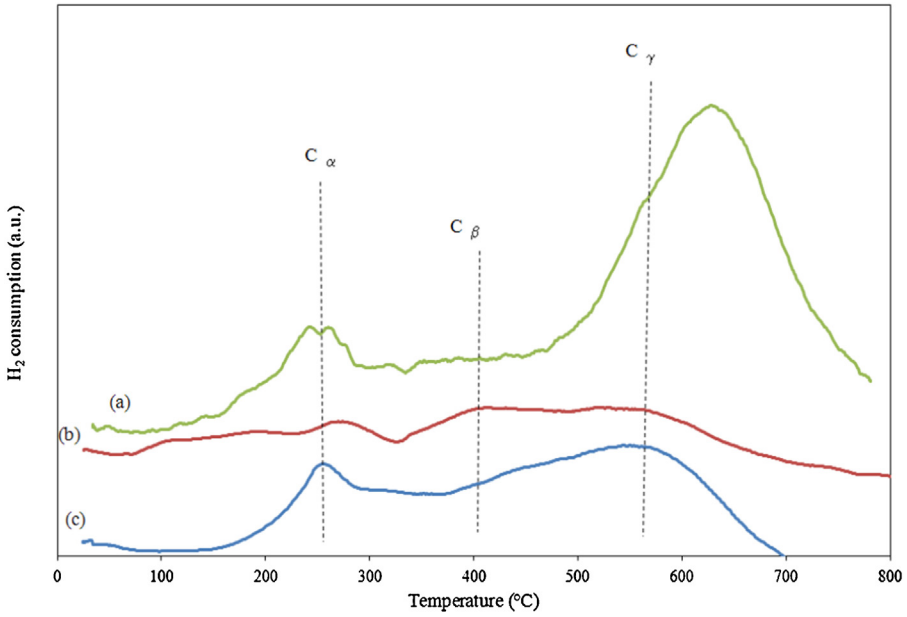

Fig. 11. TPH profiles of the catalysts after the tests at increased CH_4/CO_2 molar ratio with the different catalysts [(a) $Ce_{0.70}La_{0.20}Ni_{0.10}O_{2-\delta}$; (b) $Ce_{0.40}La_{0.40}Ni_{0.20}O_{2-\delta}$; and (c) $Ce_{0.25}La_{0.50}Ni_{0.25}O_{2-\delta}$].

after about 6 h of reaction at the fixed inlet concentration, the reagents flows where progressively changed in order to obtain different CH_4/CO_2 molar ratios, maintaining the same H_2O/CO_2 and O_2/CH_4 ratios, the results are evidenced in Fig. 9. Aim of this test is to evaluate the tolerance against fluctuation of operating conditions, namely, the range of CH_4/CO_2 molar ratios within which the catalysts can operate without sensitive decay. As highlight in Fig. 9a, during the test at lower CH_4/CO_2 ratios, the $Ce_{0.70}La_{0.20}Ni_{0.10}O_{2-\delta}$ sample shows stable performance, with a progressive increase in the CH_4 and CO_2 conversion rates by increasing the CH_4/CO_2 ratio in the feed. Whereas, at high CH_4/CO_2 molar ratio (2.47) a light decay in the catalyst performance is observed along the time on stream.

The H_2O conversion rate (not showed) follows the same trend of the CH_4 and CO_2 conversion rates: increases by increasing the CH_4/CO_2 ratio, but the moles of converted steam result lower than the CH_4 and CO_2 reacted. This evidence suggests the occurrence of RWGS reaction simultaneously with reforming reactions. In order to verify this, the apparent equilibrium constant for the water gas shift reaction (K_{exp}), from the concentration of the appropriate gases in the effluent stream, is evaluated. The derived K_{exp} values result slightly higher than the equilibrium constant for the WGS reaction, calculated from thermodynamic parameters ($K_{WGS} = \exp -\Delta G^{\circ}/RT$ at $T = 800\,^{\circ}C$), confirming that the approach to equilibrium for the water gas shift reaction is from the $CO_2 + H_2$ side.

The remaining samples (Fig. 9b and c) show analogous behavior, while a moderate decay in the performance (CH_4 and CO_2 conversion rate) during time on stream is already denoted at a CH_4/CO_2 ratio of 2.26 with $Ce_{0.40}La_{0.40}Ni_{0.20}O_{2-\delta}$ sample (Fig. 9b); while a more considerable loss of activity is observed with the last $Ce_{0.25}La_{0.50}Ni_{0.25}O_{2-\delta}$ sample, for all the investigated CH_4/CO_2 ratios, as evidenced in Fig. 9c. The related H_2/CO ratio, primarily ruled by the constant H_2O/CO_2 ratio in the feed, shows a light increase by increasing the CH_4/CO_2 molar ratio, as depicted in Fig. 10. Besides the pressure drop measured during the time on stream, invariant in the tests at low CH_4/CO_2 ratios, increases sensitively during the tests at CH_4/CO_2 ratio of 2.47, suggesting a considerable carbon formation under these very unfavorable conditions and strictly related to the Ni content in the catalysts. Methane cracking reaction (Eq. (4)), favored at high temperature respect to the Boudouard reaction (Eq. (5)), can be responsible of carbon deposition phenomena leading to the increase in the H_2/CO ratio in the reaction's products evidenced in Fig. 10; prevalence of craking reaction can compensate the H_2 consumption by the reverse water gas shift reaction.

CHNS analysis of spent catalysts reveals a carbon amount that increases from 14 wt% to 28 wt% by increasing the nickel content in the catalysts, confirming that the increase in the Ni particle size and the progressive decrease in the Ni–support interactions, can promote the methane cracking reaction [65]. Preliminary investigations to study the nature of deposited carbon were carried out by TPH and SEM analysis; the related TPH profiles of the worked catalysts are depicted in Fig. 11. Three hydrogenation peaks were identified on $Ce_{0.70}La_{0.20}Ni_{0.10}O_{2-\delta}$ sample at around 250 °C, 450 °C and 580 °C for the carbonaceous species designed as C_α, C_β and C_γ, respectively [77,78]. Increasing the Ni content in the catalysts the peaks became very broad, while at high Ni content the intensity of C_γ species increases noticeable and the peak shift to higher temperature. The reactivity of the carbonaceous species decreases in the order: $C_\alpha > C_\beta > C_\gamma$ and in term of inertness, C_γ species would be the hardest carbon species to be removed [79]. The current TPH results suggest that less stable α- and β-carbon species, over the catalysts surface plays a role of reactive intermediate in the catalytic activity, while the noticeable presence of hardly removed γ-carbon can be related to the deactivation of $Ce_{0.25}La_{0.50}Ni_{0.25}O_{2-\delta}$ sample.

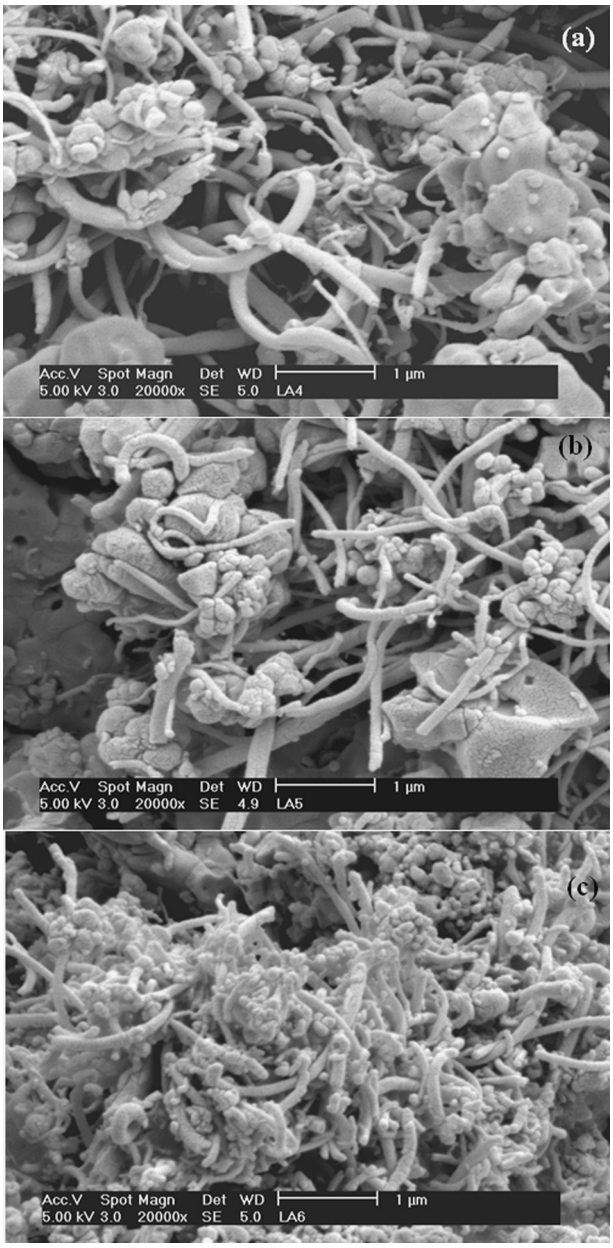

Fig. 12. SEM image of the spent catalysts after the tests at increased CH_4/CO_2 molar ratio [(a) $Ce_{0.70}La_{0.20}Ni_{0.10}O_{2-\delta}$; (b) $Ce_{0.40}La_{0.40}Ni_{0.20}O_{2-\delta}$; and (c) $Ce_{0.25}La_{0.50}Ni_{0.25}O_{2-\delta}$ samples].

SEM images of the used catalysts, shown in Fig. 12, highlight the presence of carbon as filamentous form with an abundance that increases by increasing the Ni content in the samples. Besides, a decrease in the average diameters of filamentous carbon, from 130 nm to 90 nm, by increasing the Ni content or the particle size can be observed. Generally, the growth of filamentous carbon occurs at the interface crystal to metal–support by carbon diffusion, whereby, the related particle size should be of the same order as that of the nickel particles. This apparent incongruity between Ni particle size, revealed by TEM analysis, and diameter of filamentous carbon suggests that the fibers can be covered by a consistent layer of amorphous particles. The observed decrease in the average diameter of these filaments with the increase in the Ni particle size can ascribed to a decrease in the average diameter of active nickel particle caused by the presence of oxygen and LaO_x species as ensemble size control. This surface interactions oxygen–nickel and LaO_x–nickel can restrict the active region to CH_4 adsorption causing

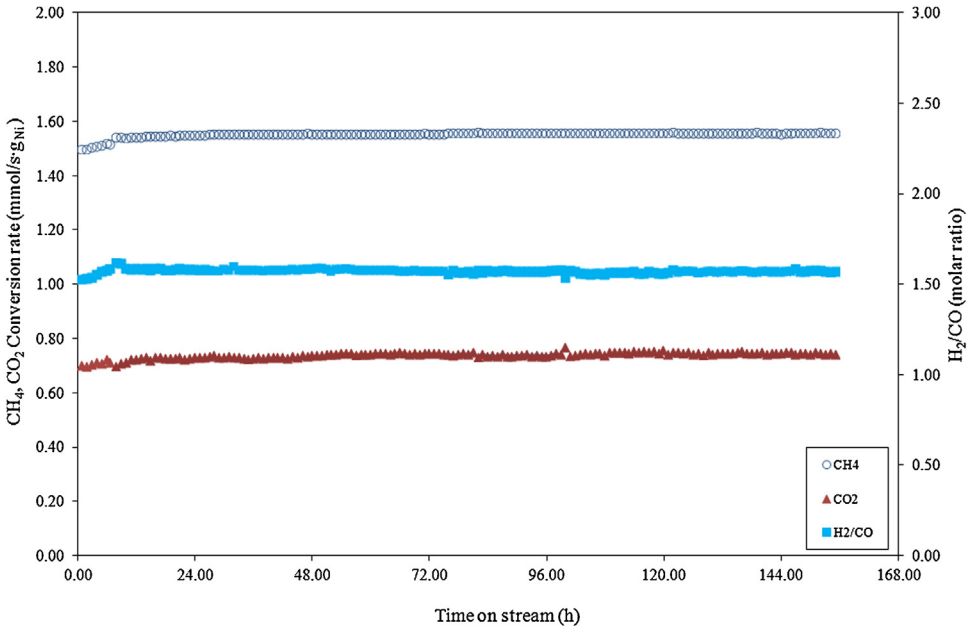

Fig. 13. Stability test with $Ce_{0.70}La_{0.20}Ni_{0.10}O_{2-\delta}$ catalyst. Reaction conditions: GHSV = 31,000 h^{-1}, T = 800 °C, CH_4:CO_2:H_2O:O_2 = 1:0.66:0.66:0.10.

a decrease in the diameter of the carbon filaments. Similar behavior has been evidenced by Dias and Assaf [80] with Ni/γ-Al_2O_3 catalyst during CH_4 steam reforming in presence of air, increasing the O_2/CH_4 molar ratio in the feed stream, a progressive decrease of carbon filaments it was observed. In the current catalysts, the decrease in the amount of oxygen vacancies by increasing Ni amount can cause a higher availability of oxygen to bond nickel; this bond limits the active region to methane adsorption that in turn can inhibit the polymerization of carbon, depending on the amount, or to determine a decrease in the diameters of the filamentous carbon.

It should be note that the present study focus the hydrogen production by tri-reforming reaction of simulated biogas (landfill gas, digester gas) that in practice contains a CH_4/CO_2 molar ratio ranging between 1.1 and 1.5 [15]. On this basis, the $Ce_{0.70}La_{0.20}Ni_{0.10}O_{2-\delta}$ sample emerges as the catalyst formulation that can ensure promising activity in the TRM reaction under a real biogas composition.

3.2.3. Catalyst stability

Performance vs. time on stream was further carried out with the selected $Ce_{0.70}La_{0.20}Ni_{0.10}O_{2-\delta}$ sample under a feed composition of CH_4:CO_2:H_2O:O_2 = 1:0.66:0.66:0.10 in order to investigate the catalyst stability, the results are depicted in Fig. 13. As shown the catalyst exhibit, after an initial period of stabilization (about 6 h), stable performance with a CH_4 conversion rate of 1.56 mmol/s g_{Ni} and CO_2 conversion rate of 0.56 mmol/s g_{Ni}, the related H_2/CO ratio reaches a value of about 1.57 during 150 h of reaction. SEM analysis of spent catalyst shows a carbon-free surface, as evidenced in Fig. 14.

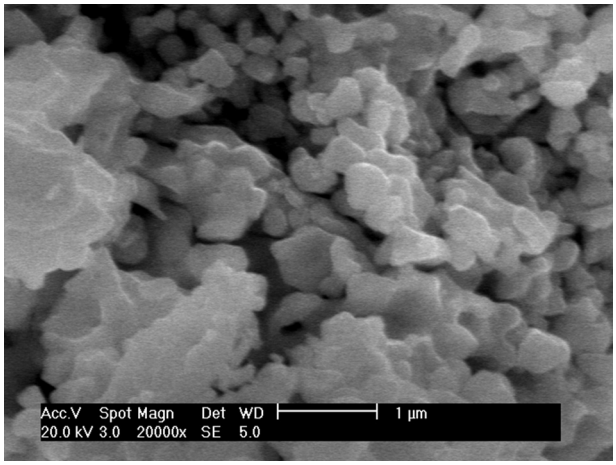

Fig. 14. SEM image of the spent catalysts ($Ce_{0.70}La_{0.20}Ni_{0.10}O_{2-\delta}$) after the stability test.

4. Conclusions

CH_4-Trireforming concept represents a new way for both conversion-utilization of CH_4 and CO_2 mixtures that can be applied to industrial flue gas as well biogas sources.

Under drastic reaction condition, as high CH_4/CO_2 molar ratios, the $Ce_{0.70}La_{0.20}Ni_{0.10}O_{2-\delta}$ sample, showed high activity and stability during 150 h of reaction carried out at 800 °C under a GHSV = 31,000 h^{-1}. The CH_4 and CO_2 conversion rates achieve 1.56 mmol/s g_{Ni} and 0.56 mmol/s g_{Ni}, respectively, producing a synthesis gas with a H_2/CO molar ratio of 1.57 in absence of carbon deposition.

The catalytic activity can be related to the interactions nickel–lanthana–surface oxygen vacancies of ceria that enhances the nickel dispersion. LaO_x species, coming from the support after the pre-reduction step, can increase the d-electron density of nickel atoms suppressing the carbon deposition. At high nickel and lanthana content, sintering and re-oxidation of active Ni-sites and/or coverage by lanthana species can induce the decay in the catalytic activity.

Acknowledgments

The authors would like to thank Dr. A.S. Aricò for his valuable discussions about XPS analysis and Mr. G. Monforte for needful technical support.

References

[1] M. Balat, Int. J. Hydrogen Energy 33 (2008) 4013–4029.
[2] C.-J. Winter, Int. Hydrogen Energy 34 (2009) S1–S52.

[3] D.J. Moon, J.M. Park, J.S. Kang, K.S. Yoo, S.I. Hong, J. Ind. Eng. Chem. 12 (2006) 149–155.
[4] J.S. Kang, D.H. Kim, S.D. Lee, S.I. Hong, D.J. Moon, Appl. Catal. A 332 (2007) 153–158.
[5] L. Maciel, A. Souza, V. Cavalcanti-Filho, A. Knoechelmann, C. Abreu, React. Kinet. Mech. Catal. 101 (2010) 407–416.
[6] D.M. Walker, S.L. Pettit, J.T. Wolan, J.N. Kuhu, Appl. Catal. A 445–446 (2012) 61–68.
[7] S.A. Solov'ev, Ye.V. Gubareni, Ya.P. Kurilets, S.N. Orlik, Theor. Exp. Chem. 48 (2012) 199–205.
[8] J.M. García-Vargas, J.L. Valverde, A. de Lucas-Consuegra, B. Gómez-Monedero, P. Sánchez, F. Dorado, Appl. Catal. A 439 (2012) 49–56.
[9] C. Song, W. Pan, Catal. Today 98 (2004) 463–484.
[10] M. Halmann, A. Steinfeld, Catal. Today 115 (2006) 170–178.
[11] S.-H. Lee, W. Cho, W.-S. Ju, B.-H. Cho, Y.-C. Lee, Y.-S. Baek, Catal. Today 87 (2003) 133–137.
[12] D. Sun, X. Li, S. Ji, L. Cao, J. Nat. Gas. Chem. 19 (2010) 369–374.
[13] M. Halmann, A. Steinfeld, Energy 31 (2006) 3171–3185.
[14] W. Cho, T. Song, A. Mitsos, J.T. McKinnon, G.H. Ko, J.E. Tolsma, D. Denholm, T. Park, Catal. Today 139 (2009) 261–267.
[15] S. Rasi, A. Vijanen, J. Rintala, Energy 32 (2007) 1375–1380.
[16] N. Muradov, F. Smith, A.T. Raissi, Int. J. Hydrogen Energy 33 (2008) 2023–2035.
[17] S.P. Hernandez, M. Chiappero, N. Russo, D. Fino, Chem. Eng. J. 176–177 (2011) 272–279.
[18] M.S. Horikawa, F. Rossi, M.L. Gimenes, C.M.M. Costo, M.G.C. de Silva, Braz. J. Chem. Eng. 21 (2004) 415–422.
[19] K. Tomoshige, Catal. Today 89 (2004) 405–418.
[20] K. Kusekabe, K.-I. Sotawa, T. Eda, Y. Iwamoto, Fuel Proc. Technol. 86 (2004) 319–326.
[21] M. Nurunnabi, B. Li, K. Kunimori, K. Suzuki, K.-I. Fujimoto, K. Tomishige, Appl. Catal. A 292 (2005) 272–280.
[22] B.C. Michael, A. Donazzi, L.D. Schmidt, J. Catal. 265 (2009) 117–129.
[23] P. Djinovic, J. Batista, A. Pintar, Int. J. Hydrogen Energy 37 (2012) 2699–2707.
[24] L.S.F. Feio, C.E. Hori, L.V. Mattos, D. Zanchet, F.B. Noronha, J.M.C. Bueno, Appl. Catal. A 348 (2008) 183–192.
[25] N. Laosiripojana, S. Assabumrungrat, Appl. Catal. A 290 (2005) 200–211.
[26] T.-J. Huang, T.-C. Yu, Catal. Lett. 102 (2005) 175–181.
[27] S.M. Lima, J.M. Assaf, M.A. Peña, J.L.G. Fierro, Appl. Catal. A 311 (2006) 94–104.
[28] H. Jiang, H. Li, H. Xu, Y. Zhang, Fuel Proc. Technol. 88 (2007) 799–995.
[29] L. Pino, A. Vita, F. Cipitì, M. Laganà, V. Recupero, Appl. Catal. B 104 (2011) 64–73.
[30] L. Barrio, A. Kubacka, G. Zhou, M. Estrella, A. Martínez-Arias, J.C. Hanson, M. Fernández-García, J.A. Rodriguez, J. Phys. Chem. C 114 (2010) 12689–12697.
[31] S. Liang, E. Broitmsn, Y. Wang, A. Cao, G. Veser, J. Mater. Sci. 46 (2011) 2928–2937.
[32] P.G. Fleming, J.D. Holmes, D.J. Otway, M.A. Morris, J. Solid State Chem. 184 (2011) 2595–2600.
[33] M.F. Wilkes, P. Hyden, A.K. Bhattacharya, Appl. Surf. Sci. 206 (2003) 12–19.
[34] V. Bellière, G. Joorst, O. Stephen, F.M.F. de Groot, B.M. Wackhuysen, J. Phys. Chem. B 110 (2006) 9984–9990.
[35] L. Liu, M. Zhang, M. Guo, X. Wang, Chin. J. Chem. Phys. 20 (2007) 711–716.
[36] K.C. Patil, M.S. Hegde, T. Ratten, S.T. Aruna, Chemistry of Nanocrystalline Oxide Materials. Combustion Synthesis, Properties and Applications, World Sci. Pub., Singapore, 2008, pp. 42–58.
[37] W. Shan, M. Luo, P. Ying, W. Shen, C. Li, Appl. Catal. A 246 (2003) 1–9.
[38] W.P. Dow, Y.P. Wang, T.-J. Huang, J. Catal. 160 (1996) 155–170.
[39] J.B. Wang, S.-Z. Hsiang, T.-J. Huang, Appl. Catal. A 146 (2003) 197–211.
[40] Y. Zhang, H. Gu, H. Chen, L. Gao, X. Zhu, L. Guo, Mater. Res. Bull. 44 (2009) 775–779.
[41] L.P. Li, G.S. Li, J. Xiang, R.I. Smith, H. Inomata, Chem. Mater. 15 (2003) 889–898.
[42] L. Pino, A. Vita, F. Cipitì, M. Laganà, V. Recupero, Catal. Lett. 122 (2008) 121–130.
[43] Y. Wang, S. Liang, A. Cao, R.L. Thompson, G. Veser, Appl. Catal. B 99 (2010) 89–95.
[44] G. Sierra-Gallego, F. Mondragón, J.-M. Tatibouët, J. Barrault, C. Batiot-Dupeyratet, Catal. Today 133–135 (2008) 200–209.
[45] B. Zhang, D. Li, X. Wang, Catal. Today 158 (2010) 348–353.
[46] X. Du, D. Zhang, L. Shi, R.G. Ao, J. Zhang, J. Phys. Chem. C 116 (2012) 10009–10016.
[47] R.M. Garcia de la Cruz, H. Falcón, M.A. Peña, J.L.G. Fierro, Appl. Catal. B 33 (2001) 45–65.
[48] A. Kumar, S. Babu, A.S. Karakoti, A. Schulte, S. Seal, Langmuir 25 (2009) 10998–11007.
[49] B.M. Reddy, L. Katta, G. Thrimurthulu, Chem. Mater. 22 (2010) 467–475.
[50] A. Serrano-Lotina, A.J. Martin, M.A. Folgado, L. Daza, Int. J. Hydrogen Energy 37 (2012) 12342–12350.
[51] M. Gorgoi, F. Schäfers, S. Svensson, N. Mårtensson, J. Electron Spectrosc. Relat. Phenom. (2013), http://dx.doi.org/10.1016/j.elspec.2013.01.004.
[52] J.F. Moulder, W.F. Stickle, P.E. Sobol, K.D. Bomben, In Handbook of X Ray Photoelectron Spectroscopy, Physical Electronics, Inc., Eden Prairie, Minnesota, USA, 1995, 0-9648124-1-X.
[53] A. Arranz, C. Palacio, Langmuir 18 (2002) 1695–1701.
[54] Y. Uwamino, T. Ishizuka, H. Yamatera, J. Electron Spectrosc. Relat. Phenom. 34 (1984) 67–78.
[55] L. Xiancai, W. Min, L. Zhihua, H. Fei, Appl. Catal. A 290 (2005) 81–86.
[56] K. Sutthiumporn, S. Kawi, Int. J. Hydrogen Energy 36 (2011) 14435–14446.
[57] S.A. Nikolaev, V.V. Smirnov, Catal. Today 147 (2009) S336–S341.
[58] J.G. Du, X.Y. Sun, G. Jiang, Eur. Phys. J. D 55 (2009) 111–120.
[59] N.S. McIntyre, M.G. Cook, Anal. Chem. 47 (1975) 2208–2213.
[60] H. Borchert, Y. Borchert, V.V. Kaichev, I.P. Prosvirin, G.M. Alikina, A.I. Lukashevich, V.I. Zaikovskii, E.M. Moroz, E.A. Paukshtis, V.I. Bukhtiyarov, V.A. Sadykov, J. Phys. Chem. B 109 (2005) 20077–20086.
[61] K. Sun, W. Lu, M. Wang, X. Xu, Appl. Catal. A 268 (2004) 107–113.
[62] F. Le Normand, J. El Fallah, H. Hilaire, P. Legaré, A. Kotani, C. Parlebas, Solid State Commun. 71 (1989) 885–889.
[63] A. Pfau, K.D. Scheierban, Surf. Sci. 321 (1994) 71–80.
[64] J. El Fallah, L. Hilaire, M. Romeo, F. Le Normand, J. Electron. Spectrosc. Relat. Phenom. 73 (1995) 89–103.
[65] J.-H. Kim, D.J. Suh, T.-J. Park, K.-I. Kim, Appl. Catal. A 197 (2000) 191–200.
[66] L.A. Rudnitskii, T.N. Solboleva, A.M. Alekseev, React. Kinet. Catal. Lett. 26 (1984) 149–151.
[67] Z. Zhang, X.E. Verykios, Catal. Today 21 (1994) 589–595.
[68] W.D. Zhang, B.S. Liu, C. Zhu, Y.L. Tian, Appl. Catal. A 292 (2005) 138–143.
[69] D. Xu, W. Li, Q. Ge, H. Xu, Fuel Proc. Technol. 86 (2005) 995–1006.
[70] X. Wang, R.J. Gorte, Catal. Lett. 73 (2001) 15.
[71] D.L. Trimm, Catal. Today 49 (1999) 3–10.
[72] W.-S. Dong, H.-S. Roh, K.-W. Jun, S.-E. Park, Y.-S. Oh, Appl. Catal. 226 (2002) 63–72.
[73] K.-Y. Shi, Q. Su, Z.-F. Zhao, H.-Y. Xu, Y.-D. Wei, G.-L. Xu, J. Nat. Gas Chem. 8 (1999) 105–114.
[74] Y. Wu, T. Yu, B.S. Dou, C.X. Wang, X.F. Xie, Z.L. Yu, S.R. Fan, Z.R. Fan, L.C. Wang, J. Catal. 120 (1989) 88.
[75] C.H. Bartholomew, Catal. Rev. Sci. Eng. 24 (1982) 67–112.
[76] S. Wang, G.Q. Lu, J. Chem. Technol. Biotechnol. 75 (2000) 589–595.
[77] J.J. Guo, H. Lou, X.M. Zhang, Carbon 45 (2007) 1314–1321.
[78] X.-Y. Quek, D. Liu, W.N.E. Cheo, H. Wang, Y. Chen, Y. Yang, Appl. Catal. A 95 (2010) 374–382.
[79] N. Wang, W. Chu, T. Zhang, X.S. Zhao, Int. J. Hydrogen Energy 37 (2012) 19–30.
[80] J.A.C. Dias, J.M. Assaf, J. Power Sources 137 (2004) 264–268.